nature photonics

SUPPLEMENTARY INFORMATION

https://doi.org/10.1038/s41566-019-0453-z

In the format provided by the authors and unedited.

Experimental realization of a Weyl exceptional ring

Alexander Cerjan[1]*, Sheng Huang[2], Mohan Wang[2], Kevin P. Chen[2], Yidong Chong[3,4] and Mikael C. Rechtsman[1]

[1]Department of Physics, The Pennsylvania State University, University Park, PA, USA. [2]Department of Electrical and Computer Engineering, University of Pittsburgh, Pittsburgh, PA, USA. [3]School of Physical and Mathematical Sciences, Nanyang Technological University, Singapore, Singapore. [4]Centre for Disruptive Photonic Technologies, Nanyang Technological University, Singapore, Singapore. *e-mail: awc19@psu.edu

Supplemental information for: Experimental realization of a Weyl exceptional ring

Alexander Cerjan,[1,*] Sheng Huang,[2] Mohan Wang,[2] Kevin P. Chen,[2] Yidong Chong,[3,4] and Mikael C. Rechtsman[1]

[1] *Department of Physics, The Pennsylvania State University, University Park, Pennsylvania 16802, USA*
[2] *Department of Electrical and Computer Engineering, University of Pittsburgh, Pittsburgh, Pennsylvania 15261, USA*
[3] *School of Physical and Mathematical Sciences, Nanyang Technological University, Singapore 637371, Singapore*
[4] *Centre for Disruptive Photonic Technologies, Nanyang Technological University, Singapore 637371, Singapore*

(Dated: May 30, 2019)

I. DERIVATION OF THE 3D WEYL EXCEPTIONAL RING HAMILTONIAN FROM THE WAVEGUIDE FLOQUET HAMILTONIAN

As discussed in the main text, the steady-state diffraction of light at a specific frequency propagating through a waveguide array is described by the paraxial approximation to Maxwell's equations. For a given electric field amplitude with a fixed linear polarization, $\mathcal{E}(x,y,z)e^{-i\omega t}$, the slowly-varying envelope, $\psi(x,y,z)$, is

$$\mathcal{E}(x,y,z) = \psi(x,y,z)e^{ik_0 z}, \tag{S1}$$

in which $k_0 = n_0\omega/c$, and n_0 is the index of refraction of the background material in the system, and the propagation is assumed to be predominantly along the z axis. In the limit that the back scattering in the z direction due to the waveguides is negligible, $\psi(x,y,z)$ satisfies the 2D Schrödinger equation,

$$i\frac{\partial\psi}{\partial z} \approx \hat{H}\psi(x,y,z) = \left[-\frac{1}{2k_0}\nabla_\perp^2 - \frac{\omega}{c}\delta n(x,y,z)\right]\psi(x,y,z), \tag{S2}$$

where $\nabla_\perp^2$ is the Laplacian in the transverse directions, x, y, and $\delta n = n - n_0$ is the shift in the refractive index which defines the waveguides. As the helical waveguides are periodic in z, with period Z, such that $\delta n(x,y,z+Z) = \delta n(x,y,z)$, Eq. (S2) is a Floquet problem whose eigenstates satisfy

$$\psi(x,y,z+Z) = e^{i\beta Z}\psi(x,y,z), \tag{S3}$$

$$\hat{H}_F\psi = \beta\psi, \tag{S4}$$

in which $\hat{H}_F$ is the Floquet Hamiltonian, and β is the Floquet quasi-energy. The Floquet Hamiltonian is defined using the z-evolution operator over a single period,

$$e^{i\hat{H}_F Z} = \mathcal{T}e^{i\int_0^Z \hat{H}(x,y,z)dz}, \tag{S5}$$

while the Floquet quasi-energy corresponds to a slight shift in the wavevector along the axis of the waveguides,

$$\beta = k_z - k_0. \tag{S6}$$

Usually, when solving for the band structure of a photonic crystal, the allowed frequencies are the eigenvalues of an equation dependent upon the wavevector components of the system, k_x, k_y, k_z. However, in re-writing Maxwell's equations using the paraxial approximation in Eq. (S2), we have effectively exchanged the wavevector component along the propagation axis, k_z, for the frequency, ω, so that the exact momentum along the waveguides' axis is now determined by the three degrees of freedom k_x, k_y, ω. Thus, when $\hat{H}_F$ is non-Hermitian, the propagation constant will develop an imaginary component, $\beta \in \mathbb{C}$, corresponding to the amplification, $\mathrm{Im}[\beta] < 0$, or attenuation, $\mathrm{Im}[\beta] > 0$, of the corresponding eigenstate, so that the total evolution of the electric field can be written as

$$E(x,y,z;t) = u(x,y,z)e^{i(k_0+\beta)z - i\omega t}, \tag{S7}$$

with $\omega \in \mathbb{R}$, and in terms of the periodic function $u(x,y,z) = e^{-i\beta z}\psi(x,y,z)$. This amplification or attenuation can instead be considered as an imaginary component of the frequency using the mode-dependent group velocity in the

* awc19@psu.edu

propagation direction, $v_{g,z}^{(n)}$, as $\Delta k_z = -\Delta\omega/v_{g,z}^{(n)}$ [1], so that the total evolution of the electric field can also be written as,

$$E(x,y,z;t) = u(x,y,z)e^{i(k_0+\tilde{\beta})z - i\tilde{\omega}t}, \tag{S8}$$

with $\tilde{\beta} = \mathrm{Re}[\beta]$, and $\tilde{\omega} = \omega - iv_{g,z}^{(n)}\mathrm{Im}[\beta]$.

The bipartite square waveguide lattice we consider here can be tuned to a topological transition at frequency ω_0, as demonstrated in the main text in Fig. 3. Thus, to lowest order in the frequency detuning, $\delta\omega = \omega - \omega_0$, in the neighbourhood of the topological transition, the Floquet Hamiltonian is described by a non-Hermitian Dirac Hamiltonian,

$$\hat{H}_F \approx v_d(\delta k_x\hat{\sigma}_x + \delta k_y\hat{\sigma}_y) + b\frac{n_0\delta\omega}{c}\hat{\sigma}_z + i\tilde{\tau}\hat{\sigma}_1 - \Delta\varepsilon\tilde{\tau}\hat{\sigma}_1, \tag{S9}$$

in which $\tilde{\tau}$ is a real number that parameterizes the loss added to the system through the breaks in one sublattice of the system, $\Delta\varepsilon$ is the effective shift in the on-site energy due to the reduction in the average index of refraction from the breaks in the waveguides per unit loss added by the breaks (hence, $\Delta\varepsilon\tilde{\tau}$ is the total decrease in the on-site energy for a given break length), $\hat{\sigma}_1 = (1/2)(\hat{\sigma}_z + \hat{I})$ is the Pauli matrix for one sublattice of the system, and v_d, b are real constants. Note that given the definition of the Floquet Hamiltonian, Eqs. (S4)-(S5), and that $\mathrm{Im}[\beta] > 0$ corresponds to attenuation in the system, $\tilde{\tau} > 0$ also corresponds to attenuation. When $\tilde{\tau} = 0$, this Floquet Hamiltonian becomes the traditional Hermitian Dirac Hamiltonian with an effective mass determined by the frequency, with the topological transition occurring at $\delta\omega = 0$. But, when $\tilde{\tau} > 0$, the system develops both an on-site loss and on-site energy shift in one of the two sublattices.

To prove that this Floquet Hamiltonian is equivalent to the non-Hermitian Weyl Hamiltonian in Eq. (1) of the main text, we must re-arrange Eq. (S9) into a form where δk_z appears as a parameter and that generates the eigenvalues $\delta\omega$. Noting that

$$\beta = \delta k_z - \frac{n_0}{c}\delta\omega, \tag{S10}$$

where $\delta k_z = k_z - n_0\omega_0/c$, we can rewrite Eq. (S4) using Eq. (S9) as

$$\left[v_d(\delta k_x\hat{\sigma}_x + \delta k_y\hat{\sigma}_y) - \delta k_z\hat{I} + \frac{\tilde{\tau}}{2}(i - \Delta\varepsilon)(\hat{\sigma}_z + \hat{I})\right]\psi = -(\hat{I} + b\hat{\sigma}_z)\frac{n_0\delta\omega}{c}\psi. \tag{S11}$$

Equation (S11) has the form of a generalized eigenvalue problem. To convert it to an ordinary eigenvalue problem, we seek to factorize the operator on the right-hand side of the equation and rescale the eigenstate vectors as,

$$\varphi = \hat{\mathcal{W}}\psi, \tag{S12}$$

$$\hat{\mathcal{W}}^2 \equiv -\frac{n_0}{c}(\hat{I} + b\hat{\sigma}_z), \tag{S13}$$

which leads to

$$\hat{H}'\varphi = \delta\omega\varphi, \tag{S14}$$

$$\hat{H}' = \hat{\mathcal{W}}^{-1}\left[v_d(\delta k_x\hat{\sigma}_x + \delta k_y\hat{\sigma}_y) - \delta k_z\hat{I} + \frac{\tilde{\tau}}{2}(i - \Delta\varepsilon)(\hat{\sigma}_z + \hat{I})\right]\hat{\mathcal{W}}^{-1}. \tag{S15}$$

Assuming that $|b| < 1$, one can directly verify that the appropriate re-scaling operators are

$$\hat{\mathcal{W}} = i\left(\frac{n_0}{2c}(1 - \sqrt{1-b^2})\right)^{1/2}\hat{I} + i\left(\frac{n_0}{2c}(1 + \sqrt{1-b^2})\right)^{1/2}\hat{\sigma}_z, \tag{S16}$$

$$\hat{\mathcal{W}}^{-1} = \frac{c}{n_0\sqrt{1-b^2}}\left[i\left(\frac{n_0}{2c}(1 - \sqrt{1-b^2})\right)^{1/2}\hat{I} - i\left(\frac{n_0}{2c}(1 + \sqrt{1-b^2})\right)^{1/2}\hat{\sigma}_z\right], \tag{S17}$$

the same as was previously reported for the Hermitian version of this system [2]. Equation (S15) can now be rewritten as

$$\hat{H}' = \frac{cv_d}{n_0(1-b^2)}(\delta k_x\hat{\sigma}_x + \delta k_y\hat{\sigma}_y) + \frac{c}{n_0(1-b^2)}\delta k_z(\hat{I} - |b|\hat{\sigma}_z) - \frac{\tilde{\tau}(i - \Delta\varepsilon)}{2}\left(\frac{c(1-|b|)}{n_0(1-b^2)}\right)\left[\hat{\sigma}_z + \hat{I}\right], \tag{S18}$$

which can be simplified by defining

$$v_\perp = \frac{cv_d}{n_0\sqrt{1-b^2}} \tag{S19}$$

$$v_z = \frac{c}{n_0(1-b^2)} \tag{S20}$$

$$\tau = \frac{\tilde{\tau}(1-|b|)}{2} \tag{S21}$$

to

$$\hat{H}' = v_\perp(\delta k_x\hat{\sigma}_x + \delta k_y\hat{\sigma}_y) + v_z\delta k_z(\hat{I} - |b|\hat{\sigma}_z) - v_z\tau(i-\Delta\varepsilon)(\hat{\sigma}_z + \hat{I}). \tag{S22}$$

This is the non-Hermitian Weyl Hamiltonian. Written in this manner, it is clear that $\Delta\varepsilon\tau\hat{\sigma}_z$ is a Hermitian perturbation to the system which has the effect of changing the location of the topological transition in k_z, while terms proportional to $\hat{I}$ amount to an overall shift in the spectrum of the system and do not play a role in the formation of either the Weyl point (when $\tau = 0$) or the Weyl exceptional ring (when $\tau > 0$). As such, these terms have been omitted from Eq. (1) of the main text, although the effect of $\Delta\varepsilon\tau\hat{\sigma}_z$ is discussed in the context of Fig. 3 of the main text, and in more detail in Sec. VI of the supplementary information.

Finally, to justify that $|b| < 1$ for this system, we provide an analysis of its order of magnitude. Recall from Eq. (S9) that b scales the effective mass in the Dirac Hamiltonian. The unbroken Hermitian system exhibits a Weyl point at $\lambda_{\mathrm{WP}} = 1609$nm. If the system is detuned to $\lambda_2 = 1564$nm, the isofrequency surfaces split at $k_x = k_y = 0$, with $\Delta k_z Z \approx \pi/4$, with Δk_z being the splitting between the upper and lower bands. This split is due to the effective mass in the system, i.e. $bn_0\delta\omega/c = \pi/8Z$. Using the identities $k_0 = n_0\omega/c = 2\pi/\lambda$, and $\delta\omega = (2\pi c/n_0)(\lambda_2^{-1} - \lambda_{\mathrm{WP}}^{-1})$, one can estimate $b = 3.5\cdot 10^{-5}$.

Throughout our analysis, we have focused only on those modes which are localized within, and propagate along, the single mode waveguides which comprise the helical waveguide array. When breaks are added to the waveguides, these waveguide modes couple to 'unbound' modes of the system that exist predominantly in the space between the waveguides. Since we only monitor the light localized to the bound modes of the waveguides at the output facet, we observe an effective loss rate for the broken waveguides. When solving for the three-dimensional band structure $\omega(k_x, k_y, k_z)$, this effective loss results in presence of the WER, despite the fact that the perturbation associated with the breaks between waveguides is purely dielectric and requires no absorptive medium.

II. PROOF OF QUANTIZED BERRY CHARGE ON A WEYL EXCEPTIONAL RING

In this section, we give an analytic proof that the non-Hermitian Weyl exceptional ring Hamiltonian of the form in Eq. (1) of the main text possess a real, quantized Berry charge. This proof is provided for completeness of this work, but its existence has been previously reported [3, 4]. To begin, we rewrite Eq. (1) as

$$\hat{H} = \tilde{k}_x\hat{\sigma}_x + \tilde{k}_y\hat{\sigma}_y + \tilde{k}_z\hat{\sigma}_z + i\tau\hat{\sigma}_z \tag{S23}$$

in which we have defined $\tilde{k}_x = v_\perp\delta k_x$, $\tilde{k}_y = v_\perp\delta k_y$, $\tilde{k}_z = -v_z|b|\delta k_z$, and $-v_z\tau \to \tau$ for simplicity, as well as dropped the two terms proportional to $\hat{I}$ as these terms only result in a global shift of the eigenvalues of the system and do not effect the eigenstates. The eigenvalues of Eq. (S23) can be quickly calculated as

$$\lambda_\pm = \pm\sqrt{\tilde{k}_x^2 + \tilde{k}_y^2 + \tilde{k}_z^2 - \tau^2 + 2i\tau\tilde{k}_z} \equiv \pm\lambda_0. \tag{S24}$$

As Eq. (S23) is a non-Hermitian Hamiltonian, it possesses left and right eigenvectors,

$$\hat{H}|\psi_\pm^R\rangle = \lambda_\pm|\psi_\pm^R\rangle, \tag{S25}$$

$$\langle\psi_\pm^L|\hat{H} = \lambda_\pm\langle\psi_\pm^L|, \tag{S26}$$

which can be calculated as

$$|\psi_\pm^R(\mathbf{k})\rangle = \left(\frac{1}{N_\pm}\right)\left(\tilde{k}_x - i\tilde{k}_y, -(\tilde{k}_z + i\tau - \lambda_\pm)\right)^T, \tag{S27}$$

$$\langle\psi_\pm^L(\mathbf{k})| = \left(\frac{1}{N_\pm}\right)\left(\tilde{k}_x + i\tilde{k}_y, -(\tilde{k}_z + i\tau - \lambda_\pm)\right), \tag{S28}$$

in which the normalization factor $N_\pm$ is

$$N_\pm^2(\mathbf{k}) = 2(\tilde{k}_x^2 + \tilde{k}_y^2 + (\tilde{k}_z + i\tau)^2) \mp 2(\tilde{k}_z + i\tau)\lambda_0, \tag{S29}$$

and ensures that $\langle \psi_i^L | \psi_j^R \rangle = \delta_{ij}$. Note that there is no simple relationship between the left and right eigenvalues of the Weyl exceptional ring Hamiltonian, which is a consequence of the fact that there is no simple symmetry (such as PT) present in systems which exhibit Weyl exceptional rings.

To calculate the Berry charge of the Weyl exceptional ring Hamiltonian, one first must decide on the proper non-Hermitian definitions of the Berry connection, $\mathbf{A}(\mathbf{k})$, and curvature, $\mathbf{\Omega}(\mathbf{k})$. In principle, there are four possibilities for these definitions stemming from different combinations of the left and right eigenvectors,

$$\mathbf{A}_\pm^{(L/R),(L/R)}(\mathbf{k}) = i\langle \psi_\pm^{(L/R)}(\mathbf{k}) | \nabla_{\mathbf{k}} | \psi_\pm^{(L/R)}(\mathbf{k}) \rangle. \tag{S30}$$

Locally, each of these are different quantities. However, it can be shown that upon defining the Berry curvature, and integrating the curvature on a closed surface, that the resulting topological charge is invariant to different choices of definition of Eq. (S30) [5]. Thus, here we adopt the choice of $A_\pm^{LR} = i\langle \psi_\pm^L | \nabla_{\mathbf{k}} | \psi_\pm^R \rangle$, from which the Berry curvature is defined as

$$\mathbf{\Omega}_\pm^{LR}(\mathbf{k}) = \nabla_{\mathbf{k}} \times \mathbf{A}_\pm^{LR}(\mathbf{k}), \tag{S31}$$

from which the Berry charge can be calculated as

$$\gamma_\pm = \frac{1}{2\pi} \int_S \mathbf{\Omega}_\pm^{LR} \cdot d\mathbf{S}. \tag{S32}$$

Finally, it will be convenient to choose the surface of integration in Eq. (S32) as a sphere with radius $\tilde{k}_R$, so we define $\tilde{k}_x = \tilde{k}_r \sin(\theta)\cos(\phi)$, $\tilde{k}_y = \tilde{k}_r \sin(\theta)\sin(\phi)$, $\tilde{k}_z = \tilde{k}_r \cos(\theta)$, and $\tilde{k}_r = \sqrt{\tilde{k}_x^2 + \tilde{k}_y^2 + \tilde{k}_z^2}$.

A. Berry charge when $|\tau| < \tilde{k}_R$

For $|\tau| < \tilde{k}_R$, the Weyl exceptional ring is entirely contained within the surface of integration, and the two eigenstates as defined in Eqs. (S27) and (S28) remain distinct. As such, using the definitions in Eqs. (S30) and (S31), the Berry connection and curvature can be calculated for the Weyl exceptional ring Hamiltonian, Eq. (S23), as

$$\mathbf{A}_\pm^{LR}(\mathbf{k}) = \frac{-\tilde{k}_y \hat{\mathbf{x}}}{N_\pm^2} + \frac{\tilde{k}_x \hat{\mathbf{y}}}{N_\pm^2}, \tag{S33}$$

and

$$\mathbf{\Omega}_\pm^{LR}(\mathbf{k}) = \mp \frac{\tilde{\mathbf{k}}}{2\lambda_0^3} \mp \frac{i\tau \hat{\mathbf{z}}}{2\lambda_0^3}. \tag{S34}$$

Using the Berry curvature and Eq. (S32), the Berry charge can then be solved for as

$$\gamma_\pm = \frac{1}{2\pi} \int_S \hat{\mathbf{r}} \cdot \mathbf{\Omega}_\pm^{LR}(\mathbf{k}) \tilde{k}_R^2 \sin(\theta) d\theta d\phi, \tag{S35}$$

which leads to the pair of integrals,

$$\gamma_\pm = \mp \frac{\tilde{k}_R^2}{2} \left[\tilde{k}_R \int_0^\pi \frac{\sin(\theta) d\theta}{\left(\tilde{k}_R^2 - \tau^2 + 2i\tau \tilde{k}_R \cos(\theta) \right)^{3/2}} + i\tau \int_0^\pi \frac{\cos(\theta)\sin(\theta) d\theta}{\left(\tilde{k}_R^2 - \tau^2 + 2i\tau \tilde{k}_R \cos(\theta) \right)^{3/2}} \right]. \tag{S36}$$

These integrals can be evaluated analytically, resulting in

$$\gamma_\pm = \mp \frac{\tilde{k}_R^2}{2} \left[\frac{i}{\tau} \left(\frac{1}{\sqrt{\tilde{k}_R^2 - \tau^2 + 2i\tau \tilde{k}_R u}} \right) \Bigg|_{u=-1}^{u=1} - \frac{i}{2\tau \tilde{k}_R^2} \left(\frac{2(\tilde{k}_R^2 - \tau^2) + 2i\tau \tilde{k}_R u}{\sqrt{\tilde{k}_R^2 - \tau^2 + 2i\tau \tilde{k}_R u}} \right) \Bigg|_{u=-1}^{u=1} \right], \tag{S37}$$

from which some additional algebra results in the final solution

$$\gamma_\pm = \mp 1 \qquad |\tau| < \tilde{k}_R. \tag{S38}$$

This proves that when the surface of integration contains the entire WER, the Berry charge of the WER is real and quantized.

B. Berry charge when $|\tau| > \tilde{k}_R$

When $|\tau| > \tilde{k}_R$, the surface of integration does not contain the WER, and instead passes through the WER. This presents an additional challenge in calculating the Berry charge, as within the exceptional ring, which is comprised entirely of branch points, the upper and lower bands can be seen to be two different portions of the same Riemann surface. Thus, we must be careful when calculating the Berry charge to correctly follow a single band of the system. By viewing the Riemann surface for this system, one can see that the correct definition of the right eigenstates within the WER is

$$|\psi_1^R\rangle = \Theta(\tilde{k}_z)|\psi_+^R\rangle + \Theta(-\tilde{k}_z)|\psi_-^R\rangle, \tag{S39}$$

$$|\psi_2^R\rangle = \Theta(\tilde{k}_z)|\psi_-^R\rangle + \Theta(-\tilde{k}_z)|\psi_+^R\rangle, \tag{S40}$$

in which $\Theta(k)$ is the Heaviside function. Using a similar definition for the left eigenstates, the Berry connection is found to be

$$\mathbf{A}_{(1,2)}^{LR}(\mathbf{k}) = \Theta(\tilde{k}_z)\mathbf{A}_{\pm}^{LR}(\mathbf{k}) + \Theta(-\tilde{k}_z)\mathbf{A}_{\mp}^{LR}(\mathbf{k}), \tag{S41}$$

with $\mathbf{A}_{\pm}^{LR}(\mathbf{k})$ given by Eq. (S33). The Berry curvature can then be calculated as

$$\mathbf{\Omega}_{(1,2)}^{LR}(\mathbf{k}) = \mp\Theta(\tilde{k}_z)\left(\frac{\tilde{\mathbf{k}}}{2\lambda_0^3} + \frac{i\tau\hat{\mathbf{z}}}{2\lambda_0^3}\right) \pm \Theta(-\tilde{k}_z)\left(\frac{\tilde{\mathbf{k}}}{2\lambda_0^3} + \frac{i\tau\hat{\mathbf{z}}}{2\lambda_0^3}\right) - \delta(\tilde{k}_z)\left(\frac{\tilde{k}_x\hat{\mathbf{x}} + \tilde{k}_y\hat{\mathbf{y}}}{N_{\pm}^2}\right) + \delta(\tilde{k}_z)\left(\frac{\tilde{k}_x\hat{\mathbf{x}} + \tilde{k}_y\hat{\mathbf{y}}}{N_{\mp}^2}\right). \tag{S42}$$

Finally, the Berry charge can be evaluated, which yields a similar set of integrals as was found in the previous case, except with extra boundary terms at the $\tilde{k}_z = 0$ plane. Upon working through the algebra, one finds that

$$\gamma_{(1,2)}^{LR} = 0 \qquad |\tau| > \tilde{k}_R. \tag{S43}$$

This completes the proof that the Berry charge on the Weyl exceptional ring remains real, quantized, and equal to that of the underlying Hermitian Weyl Hamiltonian. Although here we have only considered non-Hermiticity added with $\hat{\sigma}_z$, a more general proof can be constructed which lifts this restriction [4].

III. SIMULATION PARAMETERS

The simulations presented in this work are performed using the beam propagation method (also called the split-step method) [6, 7], which directly evolves the electric field envelope $\psi(x, y, z)$ in the propagation direction (z) in accordance with Eq. (S2). Band structures shown in Figs. 2 and 3 are propagated for a single helix pitch length Z, and then calculated using the cut and project method [8] (see the supplemental material of that work). The index variation of the waveguides is modelled as a hyper-Gaussian,

$$\Delta n(x, y, z) = \Delta n_0 e^{[(x^2/\sigma_x^2)+(y^2/\sigma_y^2)]^3}, \tag{S44}$$

for which the lengths of the axes of the waveguide's elliptical cross-section are $\sigma_x = 3.2\,\mu\text{m}$ and $\sigma_y = 4.9\,\mu\text{m}$, the background index of refraction is $n_0 = 1.473$, and the index shift of the waveguides is $\Delta n_0 = 2.6 \cdot 10^{-3}$. For ease of reproduction we repeat the remainder of the system parameters here. The transverse lattice constant is $a = 29\sqrt{2}\mu\text{m}$. The pitch of the helical waveguides is $Z = 1\,\text{cm}$. The rotation radius of the helical waveguides is $R = 4\,\mu\text{m}$.

As breaks are added to the system to induce the formation of the Weyl exceptional ring, there are 16 breaks added per helix pitch, equally spaced, each with length d_{break}, where $\Delta n(x, y, z) = 0$. Thus, for a system with $d_{\text{break}} = 60\,\mu\text{m}$, a total length of $960\,\mu\text{m}$ has been removed per Z. These breaks are arranged such that the locations in z of closest approach between neighbouring waveguides are always unbroken, and bisect the distance between adjacent breaks.

IV. LOSS AS A FUNCTION OF BREAK LENGTH

To demonstrate that these simulation parameters yield results which agree with the experiment, we compare the total transmission as a function of break length for isolated, straight waveguides. As can be seen in Fig. S1, the chosen simulation parameters faithfully reproduce the experimental results.

Moreover, we reiterate here that it is appropriate to ignore the effects of Fresnel reflection at the interfaces between the waveguides and the breaks. As the index contrast between the waveguides and the breaks is $\Delta n_0 = 2.6 \cdot 10^{-3}$,

the Fresnel reflection coefficient per interface is $\sim 10^{-6}$. Thus, for $2 \cdot 16$ interfaces per cm, the total intensity loss due to backwards reflection is $\sim 10^{-4}$ per cm. This is of a similar order to the bending losses from the rotation of the helical waveguides, but is much less than the losses incurred due to even the shortest gap lengths, which are $> 10^{-2}$ per cm, as can be seen from Fig. S1 where the intensity loss is shown for propagation distances of $L = 4.9\,\text{cm}$. Thus, Fresnel reflection constitutes a negligible source of propagation loss, and any coupling between forward and backward propagating modes can be safely ignored.

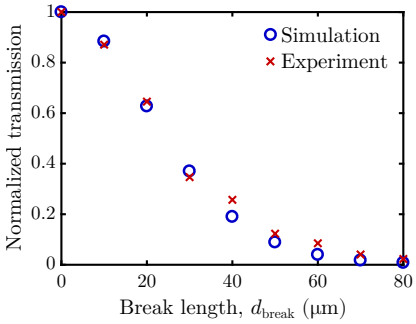

FIG. S1. **Transmission as a function of break length for isolated, straight waveguides.** Experimental results are shown as red crosses, and simulation results are shown a blue circles. The total length of the system is $L = 4.9\,\text{cm}$. For the purposes of break placement, the straight waveguides are assumed to have a fictitious helix pitch of $Z = 1\,\text{cm}$, and 16 breaks are placed per helix pitch, each with length d_{break}.

V. CONFIRMATION OF CORRECT SPATIAL DISTRIBUTION OF LOSS

In addition to the experimental observations of Fermi arc surface states and lack of conical diffraction presented in the main text, a final confirmation that the broken helical waveguide array possesses a WER can be seen in the distribution of the output power of the device between the two sublattices of the system. One consequence of adding spatially inhomogeneous loss to a system is that the system's eigenmodes localize to either the lossless or lossy regions. (In the limit of very strong loss, this localization can be proven to be perfect [9, 10].) The localization of the eigenmodes is reflected in their respective eigenvalues, which either correspond to nearly lossless or strongly attenuated propagation. This effect can be viewed as the result of an impedance mismatch between the different sublattices of the system due to the spatially inhomogeneous loss, and can lead to loss-induced transmission in waveguides [11] and reverse pump dependence in lasers [12–14]. In contrast, the eigenmodes of a Hermitian system whose elements all have the same impedance, i.e. index of refraction, are evenly distributed over the entire system. Thus, for light injected into a Hermitian bipartite waveguide array whose constituent elements all have the same index of refraction, the output power should be evenly distributed over the two sublattices of the system, yielding an output power ratio $P_A/P_B \approx 1$, where A and B denote the two sublattices of the system. However, as loss is added to the B sublattice, the propagating modes with nearly lossless transmission are localized to the lossless waveguides, instead resulting in $P_A/P_B \gg 1$. This analysis is confirmed in both simulation and experiment in Fig. S2, the Hermitian system has an output power ratio near 1, but as the break length is increased this quantity begins to diverge. This final experiment should be viewed as direct confirmation that we have achieved the non-trivial non-Hermitian term $i\tau\hat{\sigma}_z$ in Eq. (1) of the main text which results in the formation of a WER.

VI. EFFECT OF CHANGING THE INDEX OF ONE SUBLATTICE

As discussed in the main text, and above in Sec. I, one of the consequences of adding breaks to one sublattice of the helical waveguides which comprise the bipartite system is that light propagating through a break accumulates phase at a slower rate than light propagating through the corresponding region in the unbroken waveguide. Moreover, as shown in Eq. (S22), this can result in a change in the frequency, $\delta\omega$, where the topological transition occurs through the term $\Delta\varepsilon\tau$. For our system, this effective shift in the index of refraction of one of the sublattice waveguides is a non-negligible effect. For example, noting that there are 16 equally long breaks per helix pitch, if $d_{\text{break}} = 60\,\mu\text{m}$, the total length of the broken region per helix pitch is $960\,\mu\text{m}$, which is 9.6% ($Z = 1\,\text{cm}$). Thus, it is important to distinguish which features of this system are a consequence of this effective detuning of the indices of refraction of the

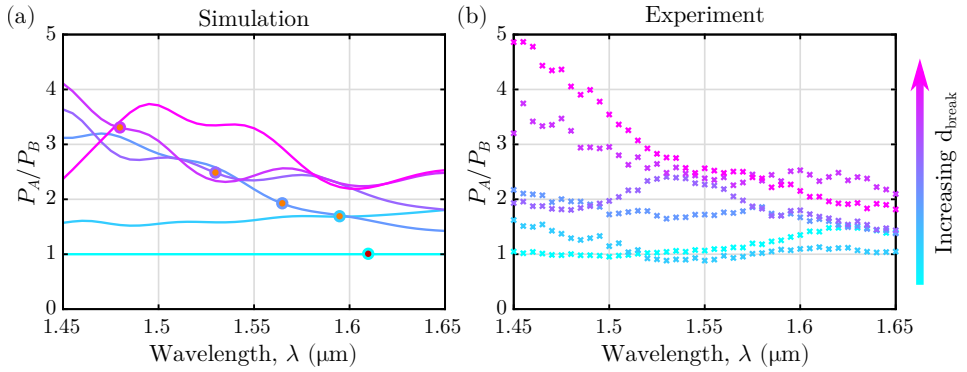

FIG. S2. **Output power ratio as a signature of a WER.** (a)-(b) Simulations and experimental observations of the sublattice power ratio, P_A/P_B, for light injected into the centre of the helical waveguide array as a function of the injected wavelength for six different break lengths $d_{\text{break}} = 0, 20, 40, 50, 60, 70\,\mu\text{m}$. The Hermitian system is shown in cyan, and redder colours indicate longer break lengths. Wavelengths where simulations predict either a Weyl point or WER are indicated in red and orange respectively.

two sublattices, a completely Hermitian phenomenon, and which features are a consequence of the loss added to the system through the inclusion of these waveguide breaks.

To disentangle the effects of the added loss from those of the index detuning, here we study systems which have the two sublattice indices detuned, but no added breaks. For example, a lossy waveguide with $d_{\text{break}} = 60\,\mu\text{m}$ and $\Delta n_B = 2.6 \cdot 10^{-3}$ has an effective index of $\Delta n_B = 2.35 \cdot 10^{-3}$ if the waveguide were unbroken, but possessing an index equal to the average index of the broken waveguide. In Fig. S3(a), we show that the wavelength of the Weyl point decreases in detuned unbroken Hermitian waveguide arrays with $\Delta n_B < \Delta n_A = 2.6 \cdot 10^{-3}$. As such, we reiterate here that the change in the wavelength of the topological transition observed in Fig. 3 of the main text is a consequence of the detuning of the indices of refraction of the two waveguides due to the added breaks in one sublattice, and not due to the loss added to the system through the breaks.

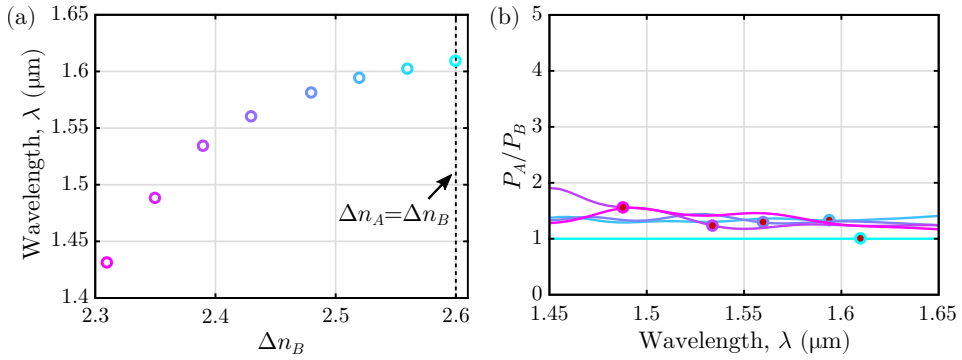

FIG. S3. **Properties of detuned, Hermitian helical waveguides.** (a) Wavelength of the Weyl point as the index detuning between the two sublattices is decreased found using full wave simulations. The values of Δn_B chosen correspond to the effective indices of refraction for $d_{\text{break}} = 0, 10, 20, 30, 40, 50, 60, 70\,\mu\text{m}$. (b) Full wave simulations of the output power ratio between the two sublattices of the detuned Hermitian system with $\Delta n_B = 2.6 \cdot 10^{-3}, 2.52 \cdot 10^{-3}, 2.43 \cdot 10^{-3}, 2.35 \cdot 10^{-3}, 2.31 \cdot 10^{-3}$ (cyan to magenta), and $\Delta n_A = 2.6 \cdot 10^{-3}$. The chosen detunings correspond to $d_{\text{break}} = 0, 20, 40, 50, 60, 70\,\mu\text{m}$.

However, the purely Hermitian change in the location of the topological transition is inconsistent with the later results in the main text. In particular, the output power ratio, P_A/P_B remains near unity for these detuned Hermitian systems, as shown in Fig. S3b, which is in sharp contrast to what is observed for the non-Hermitian systems in Fig. S2b. As such, one can conclude that while the wavelength of the topological transition is mostly determined by the effective index detuning caused by the added breaks, the added loss to one sublattice of the system has caused this detuning to realize a Weyl exceptional ring, and not a Weyl point.

VII. ADDING HOMOGENEOUS LOSS: BREAKS ADDED TO BOTH SUBLATTICES

In the previous section, we demonstrated that simply considering the Hermitian effects of adding breaks to a single sublattice of our system could not explain our observed results. Here, we consider the opposite case in which equal length breaks are added to both sublattices of the system. As such, the effective indices of both waveguides are the same, as is the added loss. This amounts to a 'trivial' addition of non-Hermiticity to the system, in the form of $i\tau\hat{I}$ within Eq. (S9) rather than $i\tau\hat{\sigma}_1$, and thus should *not* result in the formation of a Weyl exceptional ring. To confirm this, we show simulations of both the transverse radial propagation, $\langle\psi|\mathbf{r}_\perp|\psi\rangle$, and the output power ratio, P_A/P_B, in Fig. S4, for waveguide arrays with breaks added to both sublattices. This approximately doubles the loss per unit cell, so we halve the lengths of the breaks in these systems relative to those studied in the main text with breaks added to only a single sublattice.

As can be seen in Fig. S4(a), this uniform addition of loss to the system preserves the Weyl point of the system, as exhibited by a peak in the transverse radial propagation. The slight shift in the Weyl point's wavelength is due to the slight shift in the effective indices of the waveguides of the system, which changes the effective coupling constant between the waveguides, but which remain in tune as breaks have been added to both waveguides. Moreover, as loss has been added to both sublattices, the output power remains equal in both sublattices for all of the simulated break lengths, as shown in Fig. S4(b). These simulations provide further proof that adding breaks to only one sublattice of the helical waveguide array results in the formation of a Weyl exceptional ring.

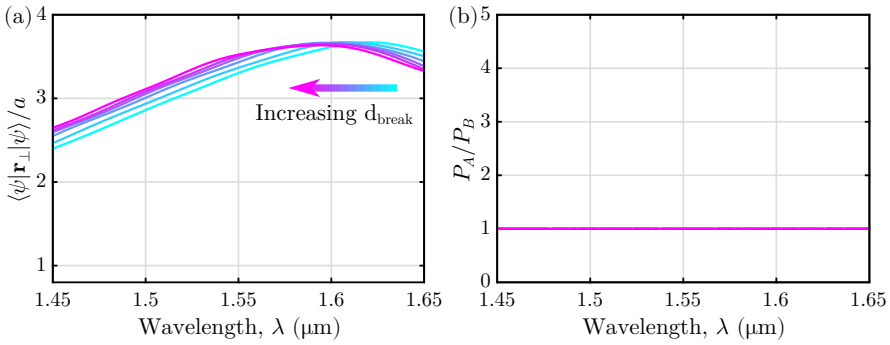

FIG. S4. **Non-Hermitian waveguide arrays with breaks added to both sublattices.** (a) Full wave simulations of transverse radial propagation and (b) output power ratio as a function of the wavelength for $d_{\text{break}} = 0, 10, 20, 25, 30, 35\,\mu\text{m}$.

[1] Joannopoulos, J.D., Johnson, S.G., Winn, J.N. & Meade, R.D. *Photonic Crystals: Molding the Flow of Light (Second Edition)* (Princeton University Press, 2011).
[2] Noh, J. *et al.* Experimental observation of optical Weyl points and Fermi arc-like surface states. *Nat. Phys.* **13**, 611 (2017).
[3] Xu, Y., Wang, S.-T. & Duan, L.-M. Weyl Exceptional Rings in a Three-Dimensional Dissipative Cold Atomic Gas. *Phys. Rev. Lett.* **118**, 045701 (2017).
[4] Cerjan, A., Xiao, M., Yuan, L. & Fan, S. Effects of non-hermitian perturbations on weyl hamiltonians with arbitrary topological charges. *Phys. Rev. B* **97**, 075128 (2018).
[5] Shen, H., Zhen, B. & Fu, L. Topological Band Theory for Non-Hermitian Hamiltonians. *Phys. Rev. Lett.* **120**, 146402 (2018).
[6] Taha, T.R. & Ablowitz, M.I. Analytical and numerical aspects of certain nonlinear evolution equations. II. Numerical, nonlinear Schrdinger equation. *J. Comput. Phys.* **55**, 203–230 (1984).
[7] Agrawal, G. *Nonlinear Fiber Optics* (Academic Press, Amsterdam, 2012), 5th edn.
[8] Leykam, D., Rechtsman, M. & Chong, Y. Anomalous Topological Phases and Unpaired Dirac Cones in Photonic Floquet Topological Insulators. *Phys. Rev. Lett.* **117**, 013902 (2016).
[9] Figotin, A. & Welters, A. Dissipative properties of systems composed of high-loss and lossless components. *Journal of Mathematical Physics* **53**, 123508 (2012).
[10] Cerjan, A. & Fan, S. Eigenvalue dynamics in the presence of nonuniform gain and loss. *Phys. Rev. A* **94**, 033857 (2016).
[11] Guo, A. *et al.* Observation of $\mathcal{PT}$-Symmetry Breaking in Complex Optical Potentials. *Phys. Rev. Lett.* **103**, 093902 (2009).
[12] Liertzer, M. *et al.* Pump-Induced Exceptional Points in Lasers. *Phys. Rev. Lett.* **108**, 173901 (2012).
[13] Brandstetter, M. *et al.* Reversing the pump dependence of a laser at an exceptional point. *Nat. Commun.* **5**, 4034 (2014).
[14] Peng, B. *et al.* Loss-induced suppression and revival of lasing. *Science* **346**, 328–332 (2014).